The Astronomical Journal, 134:1679–1692, 2007 October

THE THREE-DIMENSIONAL IONIZATION STRUCTURE AND EVOLUTION OF NGC 6720, THE RING NEBULA[1,2]

C. R. O'Dell
Department of Physics and Astronomy, Vanderbilt University, Box 1807-B, Nashville, TN 37235, USA; cr.odell@vanderbilt.edu

F. Sabbadin
INAF-Astronomical Observatory of Padua, Vicolo dell'Osservatorio 5, 35122 Padua, Italy

and

W. J. Henney
Centro de Radioastronomía y Astrofísica, UNAM Campus Morelia, A.P. 3-72, 58090 Morelia, Michaoacán, Mexico
Received 2007 May 16; accepted 2007 July 9

ABSTRACT

We have determined the gas kinematics, diagnostic and ionic radial profiles, spatial structure, and evolutionary phase of NGC 6720 (the Ring Nebula) by means of tomography and a three-dimensional recovery technique applied to long-slit high-resolution spectra. The main shell of the Ring Nebula is a triaxial ellipsoid (radii of 0.10, 0.13, and 0.20 pc) seen nearly pole-on and expanding in an approximately ballistic fashion ($V_{\rm exp} = 0.65$ km s^{-1} arcsec^{-1}). The central star characteristics [log $(L_*/L_\odot) \simeq 2.3$, $T_* \simeq 120{,}000$ K], combined with the nebular age of 7000 yr, indicate that the $M_* \simeq 0.61$–$0.62\ M_\odot$ post-AGB star is approaching the white dwarf cooling sequence. The equator of the Ring Nebula is optically thick and much denser than the optically thin poles. The inner halo surrounding NGC 6720 represents the pole-on projection of the AGB wind at high latitudes (circumpolar) directly ionized by the central star, whereas the outer, fainter, and circular halo is the projection of the recombining AGB wind at mean to low latitudes, shadowed by the main nebula. The spatio-kinematical properties of the Ring Nebula and the origin of the dense knots commonly observed in late-stage planetary nebulae are critically compared with the predictions of radiation-hydrodynamic and wind interaction models.

Key words: planetary nebulae: individual (Ring Nebula, NGC 6720)

Online material: color figures, mpeg animation

1. INTRODUCTION

The three-dimensional (3D) structure of a planetary nebula (PN) reflects its earlier history and gives an indication of its future. Although the class of objects called PNe is heterogeneous, most members share a common pattern of evolution. Although we cannot see significant changes in any one object, if we study multiple objects at different parts of their evolution, we believe that we can understand the gross features. A late-stage asymptotic giant branch (AGB) intermediate-mass star produces a highly extended atmosphere through a slow wind. This is followed by a fast stellar wind that begins as the star begins to rapidly increase in surface temperature. This produces a molecule-rich outer zone separated from an easily visible ionized zone by an ionization front, and in the innermost parts of the ionized zone there is a low-density inner core where material has been swept up by the fast wind. The density of the nebular gas decreases as the shell expands, whereupon a complex balance of factors determines if the nebula will retain the neutral outer zone or if all of the ejecta will be fully ionized. The factors in this balance are the decreasing density allowing the ionization boundary to expand, the increasing Lyman continuum (LyC) luminosity as the star increases in temperature making the ionization front expand, and the decrease of LyC luminosity which occurs as the star drops in bolometric luminosity as it collapses to a stable state of equilibrium as a white dwarf (which can cause the ionization front to contract). If a PN has reached the stage where the initial growth of the ionization front has stopped and then possibly reversed, we refer to this as a "recombined" PN. Eventually the decrease of density caused by expansion prevails, and the ionization front advances into the neutral material as the central star slowly cools. In this paper we refer to this as a "late-stage" PN. By these definitions the late-stage PN is an older PN within the recombined PN group.

As the star begins to drop in bolometric luminosity the fast wind stops, removing the driving force for the central density minimum, and the structure of the innermost parts of the nebula becomes more complex. The high-temperature inner core no longer has its sustaining stellar wind, and there is the possibility of this inner core being filled by backflowing material that lies further out. A common perception is that the low-density inner zone persists until the end of the PN evolution. This is a misperception caused by the difficulty of detecting the material there. The inner region is highly ionized and is best seen in the He II λ4686 recombination line, and most images do not include that line, thus giving the impression that the inner form still looks like the younger PNe. Images in He II λ4686 should dispel this misperception, as they reveal that in objects like the Ring Nebula in Lyra (NGC 6720) there is an inner dense zone, and in the case of the larger and older Helix Nebula (NGC 7293) the density of He II peaks at the very center of the nebula (O'Dell 1998; O'Dell et al. 2002). Although all PNe follow the same basic pattern, the timescale over which the evolution of the central star occurs is highly

[1] Based on observations at the San Pedro Mártir Observatory operated by the Universidad Nacional Autónoma de México.

[2] Based on observations with the NASA/ESA *Hubble Space Telescope*, obtained at the Space Telescope Science Institute, which is operated by the Association of Universities for Research in Astronomy, Inc., under NASA contract NAS5-26555.

dependent on the mass of that star, the evolution occurring more rapidly for the more massive stars (Blöcker 1995 and references therein). For this reason, the size and surface brightness of a PN is not a simple guide to its age, since those properties will be the total result of both the history of the nebula and the current characteristics of the central star. This situation is rendered even more complex by the fact that there are some so-called born-again PNe for which an additional mass-loss phase occurs due to instabilities when the hydrogen-deficient post-AGB star suffers a late thermal pulse during the motion toward the white dwarf region. Hydrogen mixes and burns on a convective turnover timescale, due to the pulse-induced convection (Blöcker 1995, 2001; Herwig et al. 1999) late in the star's collapse.

This scenario indicates that the past and current dynamics are what determine the form of each nebula as we now observe it. This means that to understand today's nebula, we need to understand both its form and its current velocities. Wilson (1950) observed PNe that were large and old enough to be beyond the initial phase of formation yet were not so large and of low surface brightness that they were too faint for the photographic spectrographs available to him. In these nebulae he determined that there was a well-defined velocity pattern, with the ionized material lying furthest from the central star having the greatest expansion velocity and the innermost material having the lowest, arguing that the velocities resemble what happens in homologous expansion, where the greatest distances correspond to the greatest velocities. Sometime this is referred to as a Hubble flow, in analogy with the first-order model for the expanding universe.

Within the last decade a technique has been developed for deriving the 3D structure of PNe from maps of their radial velocity structure. This has been applied to the relatively high surface brightness PNe NGC 6565 (Turatto et al. 2002), NGC 6818 (Benetti et al. 2003), NGC 7009 (Sabbadin et al. 2004), and NGC 6741 (Sabbadin et al. 2005), inferring the patterns of the structure of PNe at various phases of stellar collapse. The complexity of disentangling the star-nebula relation is underlined by the fact that NGC 7009 is kinematically the oldest nebula in the sample of Sabbadin et al. (2004), yet its central star is the least evolved and the only one showing spectroscopic evidence of a fast stellar wind.

In general it is the larger and lower surface brightness PNe (e.g., NGC 6720, NGC 6853, NGC 3587, and NGC 7293) that become the best guide to what conditions will be like as the nebulae begin to mix their material into the interstellar medium. This is particularly important since the larger PNe have trapped a significant and possibly major fraction of their material into dense knots (O'Dell et al. 2002; Meixner et al. 2005). In this paper we focus on NGC 6720 (the Ring Nebula, PNG 063.1+13.9; Acker et al. 1992).

1.1. *The Distance and Configuration of the Ring Nebula*

Although the Ring Nebula is considered a "classical" nebula because of its form, it has not been as thoroughly investigated as many more irregular-form PNe because of its lower surface brightness. It lies at a distance that presently defies an accurate determination of its trigonometric parallax, with Harris et al. (2007) finding a parallax of 1.42 ± 0.55 mas. The trigonometric distance of 700^{+450}_{-200} pc falls within the broad range of distances derived from statistical methods and is adopted in this paper.

The approximate semiminor axis of $30''$ corresponds to 0.10 pc, significantly larger than most PNe that have been studied in detail but smaller than the Helix Nebula's main disk. It has been imaged in [O III] λ5007, [N II] λ6583, and He II λ4686 emission by the *Hubble Space Telescope* (*HST*) WFPC2 camera with undersampled pixels of $0.10''$.[3] Speck et al. (2002) imaged it in the 2.12 μm H_2 line with the *HST*'s NICMOS camera at about $0.2''$ resolution, finding that most of this molecular emission arises from knots close to the ionization front. Masson (1990) first argued for the currently accepted general model of the nebula being a prolate spheroid with an equatorial enhancement of density and the axis of rotational symmetry pointed only 30° from the line of sight. Hα and radio images indicate that the density is nonzero in the center and rises with increasing distance from the central star. Bryce et al. (1994) used multislit Hα+[N II] spectra along the apparent major axis to model NGC 6720 as a bipolar nebula projected almost pole-on.

The Masson (1990) model was refined by Guerrero et al. (1997), who obtained slit spectra across three position angles and argued that the rotational axis of symmetry is about 30° from the observer and pointed toward a position angle P.A. $= 60^\circ$. The Guerrero et al. (1997) images reach fainter magnitudes than those of Lame & Pogge (1994), but the latter have a better spectral coverage. Guerrero et al. (1997) argue that the object is optically thin to LyC photons along its rotational axis and provides the source of photoionization of the outer structures with a diameter up to $230''$. Hiriart (2004) used velocity-resolved images in 2.12 μm H_2 to conclude that this emission is from a hollow cylinder seen pole-on, mapping the photodissociation regions within the knots located near the ionization front of the equatorial belt.[4] This complex picture of the inner part of the Ring Nebula occurs in the presence of an external double halo. The inner, brighter halo ($160'' \times 146''$ in diameter) consists of a variegated system of limb-brightened loops and is elongated along the apparent major axis of the main nebula. The outer, fainter halo is irregular and knotty, almost circular (about $230''$ in diameter) and with a limb-brightened rim. According to Guerrero et al. (1997), the halos of the Ring Nebula have similar chemical abundances and kinematical properties. They argue for both halos having a common origin in the slowly expanding ($V_{\rm exp} \simeq 15$ km s^{-1}) AGB wind.

1.2. *Characteristics of the Ionized Gas*

The physical conditions of the nebula have been determined by analysis of emission-line ratios. The most complete map of the electron temperature is that of Garnett & Dinerstein (2001), who used the [O III] lines. They found an average temperature of about 11,000 K, with the outer parts of the O^{++} zone having a temperature of 10,000 K and the region projecting onto the central star at almost 12,000 K.

The density determinations have been made using fluxes of suitable doublets: [N I] and [S II] for low-ionization regions, as well as [Cl III] (mean ionization) and [Ar IV] (high ionization). The mean values for the main nebula's body are

$$N_e[\text{N I}] \simeq N_e[\text{S II}] \simeq N_e[\text{Cl III}] \simeq N_e[\text{Ar IV}] = 500\text{–}700 \text{ cm}^{-3}$$

(Aller et al. 1976; Barker 1987; Lame & Pogge 1994; Liu & Barlow 1996; Guerrero et al. 1997; Garnett & Dinerstein 2001; Liu et al. 2004).

1.3. *Characteristics of the Central Star*

There is a surprising spread in the reported apparent brightness of this star. Kaler (1983) presents the unpublished photoelectric brightness of W. Liller, $B = 14.69 \pm 0.10$ and $V = 15.00 \pm 0.10$.

[3] See http://heritage.stsci.edu/1999/01/index.html.

[4] Hiriart (2004) states that the P.A. for the major axis of the cross section ellipse is 33°, rather than the correct P.A. of 57°.

Napiwotzki & Schönberner (1995) give $V = 16.2 \pm 0.3$, and Tylenda et al. (1991) and Harris et al. (2007) find $V = 15.29$ and 15.75, respectively, without reporting the uncertainty. We adopt $V = 15.75$ and Liu et al.'s (2004) extinction of $c_{\mathrm{H}\beta} \simeq 0.20$, which corresponds to a V bandpass extinction of 0.43 mag.

The spread in V magnitude contained in the literature strongly affected past determinations of the star's Zanstra temperature. Since the nebula is likely to be optically thick in all directions only in the He II continuum, the He II Zanstra temperature ($T_{\mathrm{Z\text{-}He\,II}}$) is to be preferred, being relatively insensitive to stellar model subtleties. Kaler (1983) gives $T_{\mathrm{Z\text{-}He\,II}} = 145{,}000$ K, Kaler & Jacoby (1989) 162,000 K, Malkov et al. (1995) 133,000 K, Stanghellini et al. (2002) 140,000 K, and Phillips (2003) 120,600 K. Moreover, the energy-balance method (Pottasch & Preite-Martinez 1983) provides a blackbody temperature of 115,000 K for a nebula optically thick in the He II continuum but optically thin in H-LyC. We note that Napiwotzki (1999) derives an effective temperature of $101{,}200 \pm 4600$ K and a gravity of $\log g = 6.88 \pm 0.26$ from profiles of the Hδ absorption line, a result rather model-dependent, and the uncertainties of the results are probably greater than stated.

The adopted V magnitude and extinction, together with the Hβ and He II λ4686 nebular fluxes (Barker 1987; Tylenda et al. 1994; Guerrero et al. 1997; Liu et al. 2004; and references therein), give $T_{\mathrm{Z\text{-}He\,II}} = 125{,}000 \pm 5000$ K, providing a stellar luminosity of $200^{+115}_{-80}\ L_{\odot}$.

Even with the spread in the derived temperatures and gravities and the uncertain distance, one concludes from the calculations of Schönberner (1983) and Blöcker (1995) that the central star is about $0.6\ M_{\odot}$, has passed the turn point at the end of hydrogen-shell nuclear burning, and is approaching the white dwarf cooling sequence, which is consistent with the determination of Cerruti-Sola & Perinotto (1985) that there is no spectroscopic evidence of a high-velocity stellar wind.

In this paper we present a study of this intermediate-stage PN that uses the results of radial velocity and flux mapping. The observations are described in § 2, the method of processing the spectra is in § 3, the derivation of the 3D model based on radial velocities is in § 4, the determination of the ionization structure from the pixel-to-pixel flux distribution is in § 5, and the results are discussed in § 6.

2. THE OBSERVATIONS

The new observations used in this study are long-slit spectra obtained at the Observatorio Astronómico Nacional en San Pedro Mártir operated by the Universidad Nacional Autónoma de México. We employed the MEZCAL echelle spectrograph (Meaburn et al. 2003) mounted on the 2.1 m telescope. This combination of spectrograph and telescope was nearly ideal for our program. The spectrograph was employed in a single spectral order mode by isolating each order with a narrowband interference filter. The 70 μm wide entrance slit projected 0.9″ onto the plane of the sky and was much longer than the nebula. The 24 μm pixels of the SITe 1024×1024 CCD detector were double sampled along the slit (0.62″ pixel^{-1}). The spectrum was read out in single pixels along the dispersion, giving a full width at half-maximum (FWHM) of the thorium-argon comparison lamp emission lines of 6.6–7.0 km s^{-1}. The atmospheric seeing varied from 1″ to 1.5″ during the exposures.

Observations were made over the period of 2006 June 13–17, with interruptions for clouds and smoke from nearby forest fires. The observing procedure was to select a configuration for isolating a single wavelength range and then observe the nebula with the central star centered on the slit; a sequence of double exposures (for cosmic-ray-event removal) was taken at a variety of position angles beginning with P.A. = 70°. For Hα+[N II] and [O III], a complete mapping at 10° intervals of P.A. was obtained, whereas steps of 30° were taken for He II. The slit settings are shown in Figure 1, which demonstrates that there is very complete coverage of the inner part of the nebula but that there are open gaps in the outer parts. Our method of analysis is forced to interpolate the information between the observed positions. This method gives the potential for exaggerating a small bright feature that falls within a slit setting and to underemphasize a feature falling between the slit settings.

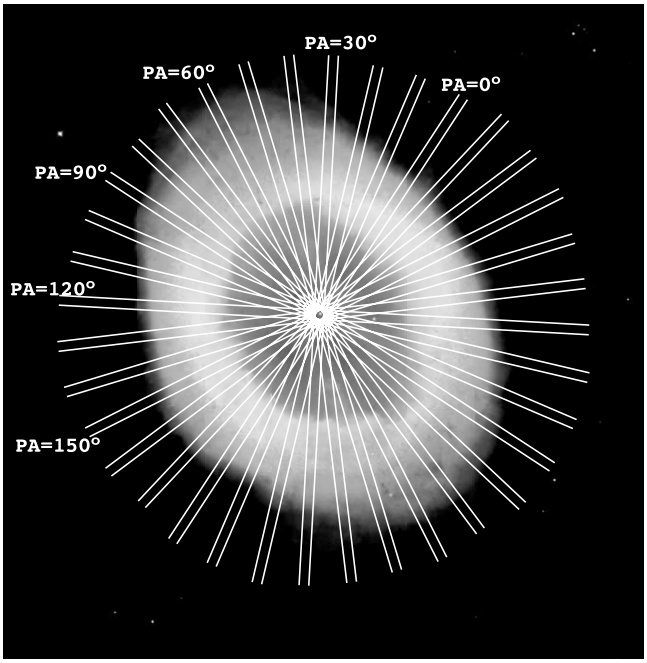

FIG. 1.— Slit settings superimposed on a 121″ × 124″ *HST* image of the Ring Nebula. The slits were actually much longer than drawn, and the width is exaggerated here for clarity, being drawn as 2″, which is comparable to the effective resolution, while the actual slits were 0.9″ wide. [*See the electronic edition of the Journal for a color version of this figure*.]

Representative samples of the spectra are shown in Figure 2. The peak signals in various lines with a gain value of 4 were about 2700 for Hα λ6563, 6500 for [N II] λ6583, 3000 for [O III] λ5007, and 90 for He II λ4686. Although the central star was always centered on the entrance slit, its position along the slit varied as different P.A. values were adopted. The 10° increments of P.A. meant that there was not continuous coverage of the entire nebula; however, it was reasonably complete, since this angle subtends 5″ at 30″ from the central star. A comparable coverage of the He II core was possible with 30° steps because of its small size. The spectral images of Figure 2 are blurred by different agents: seeing and guiding are the broadening components along the spatial axis (for an effective resolution of about 2″), whereas the velocity axis is affected by instrumental resolution, thermal motions, turbulence, the expansion gradient across the nebula, and the fine structure of recombination lines (for details, see Sabbadin et al. 2005).

3. PROCESSING THE SPECTRA

The spectra were processed using IRAF[5] tasks to correct for distortion and wavelength calibration, with the final spectra

[5] IRAF is distributed by the National Optical Astronomy Observatory, which is operated by the Association of Universities for Research in Astronomy, Inc., under cooperative agreement with the National Science Foundation.

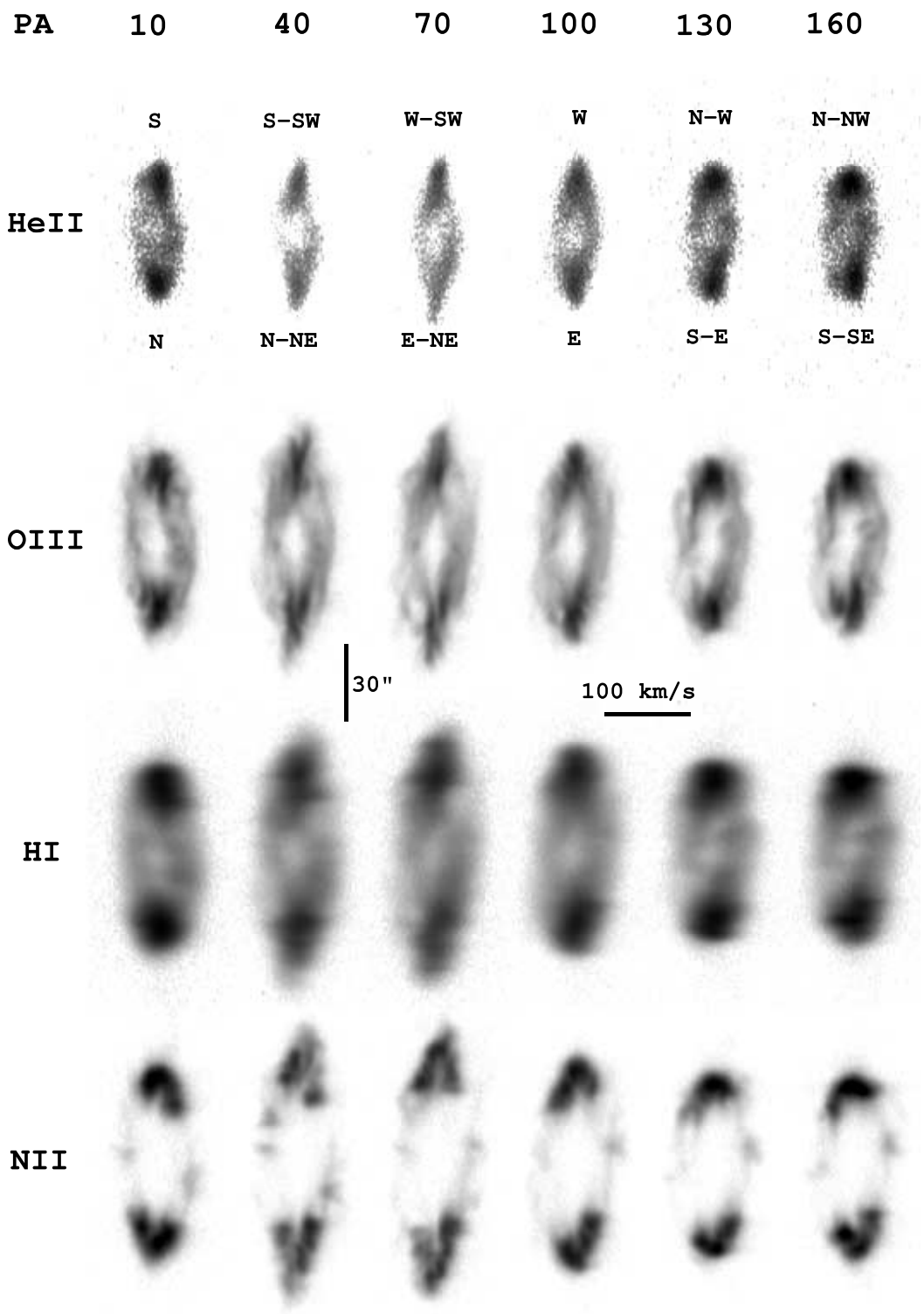

FIG. 2.— Detailed spectral image of the Ring Nebula in four ionic species (He II at 4686 Å, *first row*; [O III] at 5007 Å, *second row*; H I at 6563 Å, *third row*; [N II] at 6583 Å, *fourth row*) is shown for six equally spaced P.A.'s, including the apparent major and minor axes (P.A. = 70° and 160°, respectively). The blueshifted gas is to the left. The slit orientation at each P.A. is given in the top row, He II.

rendered into pixels of exactly 2 km s^{-1}. The at-rest wavelengths for Hα, [N II], [S II], and [O III] were those of Esteban et al. (1998), while a value of 4685.7456 Å was assumed for the He II line, as indicated for the nebula's density by Clegg et al. (1999).

In order to proceed with the analysis, as described in § 4, it was necessary to make several adjustments to the spectra. The first adjustment was a shift perpendicular to the dispersion to correct for the fact that the central star was not always located at the same position along the entrance slit. The stellar spectrum was too faint to use for this correction, so a method using the nebular emission was employed. For this purpose the monochromatic images of the nebula made with the *HST* WFPC2 were used for reference.

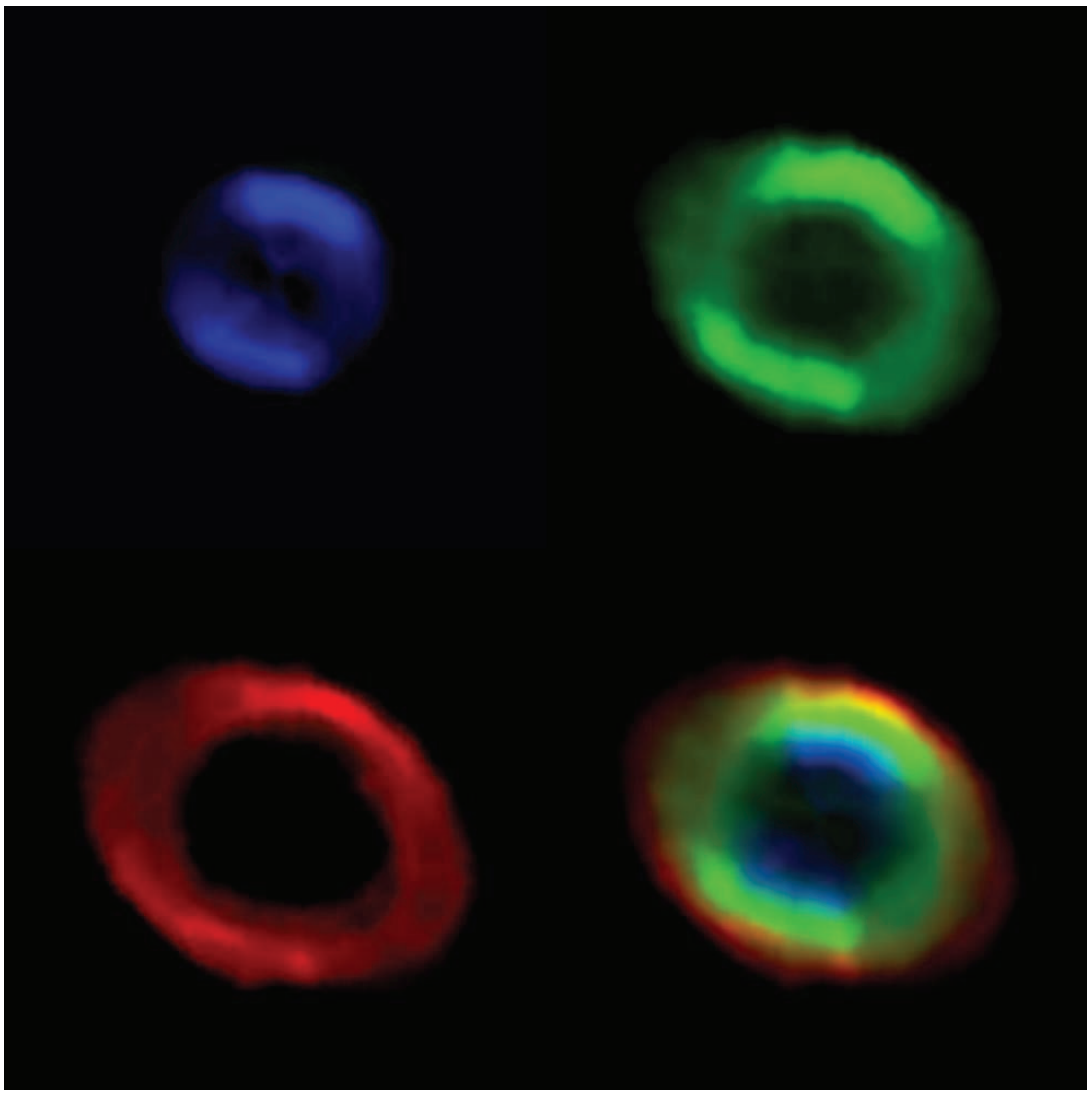

FIG. 3.—Monochromatic images of the Ring Nebula in He II (*top left*), [O III] (*top right*), [N II] (*bottom left*), and multicolor (*bottom right*) as derived by the 3D recovery program of Ragazzoni et al. (2001) applied to our spectral images. North is up, and east to the left.

The archived reference images were taken from program GO 8726 (O'Dell et al. 2002) for Hα, [N II], [S II], and He II and from GO 7632 for [O III]. The spectra were shifted until the all-velocities profile along the slit matched the profile along the corresponding P.A. on the images. A second and smaller correction was determined by creating an artificial monochromatic image from the spectra, then comparing this with the WFPC2 images. It is estimated that the uncertainty in alignment is less than 2.5 pixels (1.5″), as confirmed a posteriori by the optical appearance of the reconstructed nebula (Fig. 3).

Figure 2 emphasizes the complex structure of the Ring Nebula, with non-Gaussian line profiles probably due to blending of different velocity components (Guerrero et al. 1997).[6] The Ring Nebula presents a large stratification of the radiation and the velocity, with the brightest emissions occurring in (or close to) the plane of the sky; i.e., the nebula is seen almost pole-on. Moreover, the low-ionization [N II] lines concentrate in the dense equatorial zones and in a few small-scale, localized structures belonging to the weak circumpolar regions and projected close to the central star.

The emission lines are untilted along (and close to) the apparent minor axis (P.A. = 160°), whereas they are slightly tilted along (and close to) the apparent major axis (P.A. = 70°); the barycentric velocity of the blueshifted and redshifted merging components of [N II] and [O III] is 6 ± 2 km s^{-1} bluer in the east-northeast sector than in the west-southwest one, in agreement with the value of about 9 km s^{-1} reported by Guerrero et al. (1997).[7] The presence of a line tilt along and close to the apparent major axis indicates that the bright ring is intrinsically elliptical, and not the elliptical projection of a circular ring (in the latter case, the line tilt should be along and close to the apparent minor axis).

Since the atmospheric transmission varied during the observations, the spectra were normalized to the same effective conditions by comparison with the WFPC2 images. The resultant images were rendered into absolute flux units to within 20% by reference to the WFPC2 images after calibration using the method and results of O'Dell & Doi (1999). This flux calibration could not

[6] In Guerrero et al. (1997) the slit orientation of the right panel in Figs. 3 and 4 should be reversed.

[7] These authors probably include the prominent, unsplit, blueshifted "nose" present at the northeast edge of their [N II] spectral image in P.A. = 53° (and of our [O III] and [N II] spectral images in P.A. = 40°–70°; see Fig. 2).

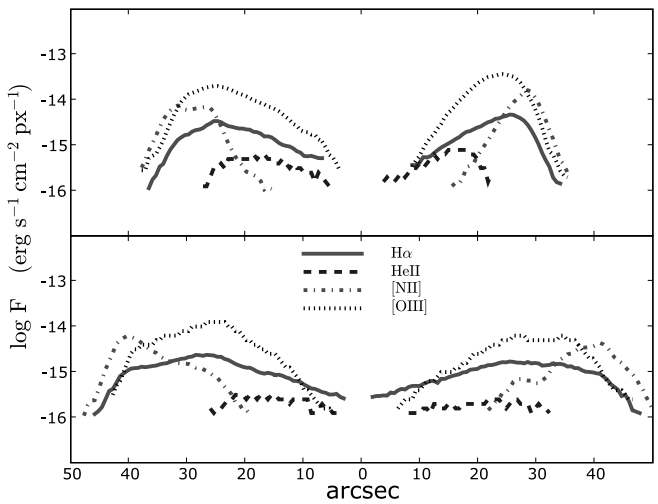

FIG. 4.— Entire zvpc flux profile of NGC 6720 (corrected for $c_{H\beta} = 0.20$) at two representative P.A.'s, sampled at intervals of 0.62″ i.e., 1 pixel. The top panel refers to the apparent minor axis (P.A. = 160°); the south-southeast sector is to the left, and the north-northwest one to the right. The bottom panel contains the apparent major axis (P.A. = 70°); the east-northeast sector is to the left, and the west-southwest one to the right. The central star position is at $X = 0.0$. [*See the electronic edition of the Journal for a color version of this figure*.]

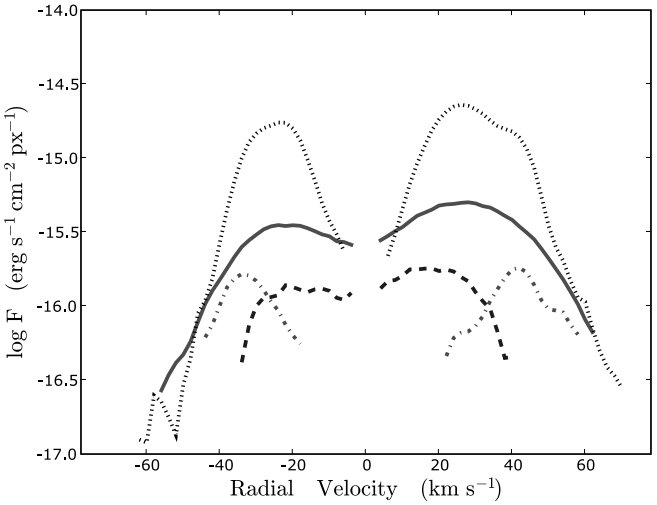

FIG. 5.— Entire cspl flux profile observed in NGC 6720 (corrected for $c_{H\beta} = 0.20$), sampled at intervals of 2.0 km s^{-1}, i.e., 1 pixel. The *X*-axis is centered at −20.0 km s^{-1}, the systemic radial velocity. Same symbols as Fig. 4. [*See the electronic edition of the Journal for a color version of this figure*.]

be used directly for the He II spectra since no on-orbit calibration of the WFPC2 F469N filter has been made. In this case we used the spectra of Hawley & Miller (1977) to tie the He II observations into the calibrated flux system. The artificial images of the nebula created from the spectral images (see § 4.3) are shown in Figure 3. These reduced-resolution images are comparable to those in Lame & Pogge (1994), who also imaged the nebula in [S II], [O I], Hα, and Hβ.

4. DERIVATION OF THE THREE-DIMENSIONAL MODEL BASED ON RADIAL VELOCITIES

We have applied the method originally introduced by Sabbadin et al. (1985, 1987) and later expanded on by multiple collaborators at the Observatory of Padua (Sabbadin et al. 2006 and references therein). In this method the spatial position, radial thickness, and ionic density of each elementary volume within a homologously expanding nebula are derived from the radial velocity, FWHM, and flux of the corresponding emission. We have applied their three-step procedure to the Ring Nebula, first deriving the radial (i.e., 1D) spatio-kinematics, then extracting tomographic (i.e., 2D) maps, and then building a spatial (i.e., 3D) reconstruction. This approach to modeling differs from that of the SHAPE method (Steffen & López 2006), which derives simulated observations from an assumed model, iterating the parameters until agreement in appearance and the available velocity data is obtained. In contrast, the Paduan approach employed here uses the velocity and emissivity at various positions to derive the 3D figure. Like SHAPE, this approach maps only the observed material, which in this case is the photoionized portion of the nebula. The detailed study of the extinction indicates that the distortion of the result due to internal extinction is nil.

4.1. *The Spatio-kinematical Properties of the Ring Nebula*

The overall spatio-kinematical properties of NGC 6720 were derived by combining the spatial profile at the systemic radial velocity (the "zero velocity pixel column" [zvpc] of the spectral images at each P.A.) with the kinematics of the gas projected at the apparent position of the star (the "central star pixel line" [cspl] of the spectra, common to all P.A.'s; Sabbadin et al. 2004 and references therein).

The zvpc selects only gas moving perpendicular to the line of sight. Under our assumption of purely radial motions, this gas will lie in the same physical plane, and hence defines a planar section through the nebula. The cspl, on the other hand, selects a pencil beam of gas along the line of sight to the star, which is at right angles to the plane selected by the zvpc.

Two representative zvpc flux profiles from along the apparent major and minor axes are shown in Figure 4. They have been corrected for extinction using $c_{H\beta} = 0.20$ (Liu et al. 2004). This illustrates the ionization stratification of the nebula. At the nebular edge, the 6583 Å line of [N II] is stronger than Hα, suggesting that the dense equatorial matter in (or close to) the plane of the sky is optically thick to the LyC of the central star.

Examination of the cspl image (Fig. 5) shows that the peak separation (corresponding to $2V_{exp}$) in the different ions is 38 ± 3 km s^{-1} for He II, 50 ± 2 km s^{-1} for [O III], 49 ± 3 km s^{-1} for Hα, and 78 ± 3 km s^{-1} for [N II], in reasonable agreement with previous values reported (Wilson 1950; Atherton et al. 1978; Bryce et al. 1994; Guerrero et al. 1997). The noise level in the two aforementioned figures is reached at log F(ergs cm^{-2} s^{-1} pixel^{-1}) = −16.8, as shown by the [O III] profile in Figure 5 (*left*).

The cspl flux profile confirms the large stratification of the kinematics along the radial direction. The [N II] emission at 6583 Å is always fainter than Hα, suggesting that the weak polar regions of the Ring Nebula are optically thin to the UV stellar radiation.

Combining the zvpc and cspl figures allows drawing several major conclusions but cannot provide the general spatio-kinematics in the two ways suggested by Sabbadin et al. (2005) for a random projected PN, since NGC 6720 is seen nearly pole-on. Our conclusions are as follows:

1. The "relative" spectral and spatial resolutions of our echellgrams are quite different: $SS = V_{exp}/\Delta V \simeq 5$ and $RR = r/\Delta r \simeq 20$ (where ΔV is the instrumental spectral resolution and Δr is the seeing+guiding). This means that the spatial information is much more accurate than the kinematical information (Ragazzoni et al. 2001), as expected from an apparently large but slowly expanding object.

2. The Hα profile in Figures 4 and 5 suggests that peak density ratios are about 7/4 for the apparent minor and major axes and approximately 7/2 for the apparent minor axis and the poles.

3. The ionized gas of NGC 6720 follows Wilson's law in that the high-excitation zones expand more slowly than the low-excitation ones, and a positive correlation exists between the expansion velocity and the size of the monochromatic image (Wilson 1950).

4. The nebula is a triaxial form seen nearly pole-on and consists of a thick, elliptical equatorial ring with thin and faint polar regions.

5. The matter density is much higher in the equatorial regions than in the poles, and we infer that R''(poles) is larger than R''(equator).

Thus, we adopt the conservative assumption

$$R''(\text{poles}) \simeq 1.5R''(\text{major axis of the equator}) \simeq 60'',$$

providing the general expansion law $V_{\rm exp}(\text{km s}^{-1}) \simeq 0.65R''$ for the ionized gas of NGC 6720.[8]

When this general expansion law is combined with the line tilt of 6 ± 2 km s^{-1} along the apparent major axis, we derive an angle of $i = 6.5^\circ \pm 2^\circ$ between the polar axis and the line of sight.[9]

4.2. *Tomography*

Figure 6 (multicolor in the electronic version) shows the complete velocity field at the six P.A.'s of Figure 2. He II, [O III], and [N II] mark the high-, medium-, and low-ionization regions. These position-velocity (P-V) maps are relative to the systemic heliocentric velocity of the nebula, $V = -20.0 \pm 1.0$ km s^{-1}, and are scaled according to $V_{\rm exp}(\text{km s}^{-1}) \simeq 0.65R''$. They represent the 2D tomographic map of each slice through the nebula at the slit setting for each P.A. Figure 5 emphasizes the complex structure of NGC 6720, the large stratification of the emitting regions, and the enhancement of the low-ionization species in the external parts of the equatorial regions and in some isolated, small-scale circumpolar structures.

4.3. *Derivation of the 3D Structure*

We selected the 4686 Å line of He II, the 5007 Å line of [O III], and the 6583 Å line of [N II] as markers of the high-, medium-, and low-ionization regions of NGC 6720, respectively. Using the techniques of Sabbadin et al. (2006), the spectral images were deconvolved for seeing, spectral resolution, and thermal motion (fine structure also was taken into account for the recombination line of He II), deprojected through the relation $V_{\rm exp}(\text{km s}^{-1}) = 0.65R''$, and assembled by means of the 3D rendering procedure described by Ragazzoni et al. (2001).

For reasons of space, only a limited number of frames are shown in the print version of this paper, corresponding to a partial rotation around the north-south axis centered on the exciting star (i.e., almost perpendicular to the polar axis of the Ring Nebula). The complete series of nebular movies is available in the electronic version of the *Astronomical Journal* and also online at a Web site dedicated to the 3D structure of expanding nebulae.[10]

Figures 7, 8, and 9 contain the opaque reconstruction of NGC 6720 in He II, [O III], and [N II] at high-, mean-, and low-flux

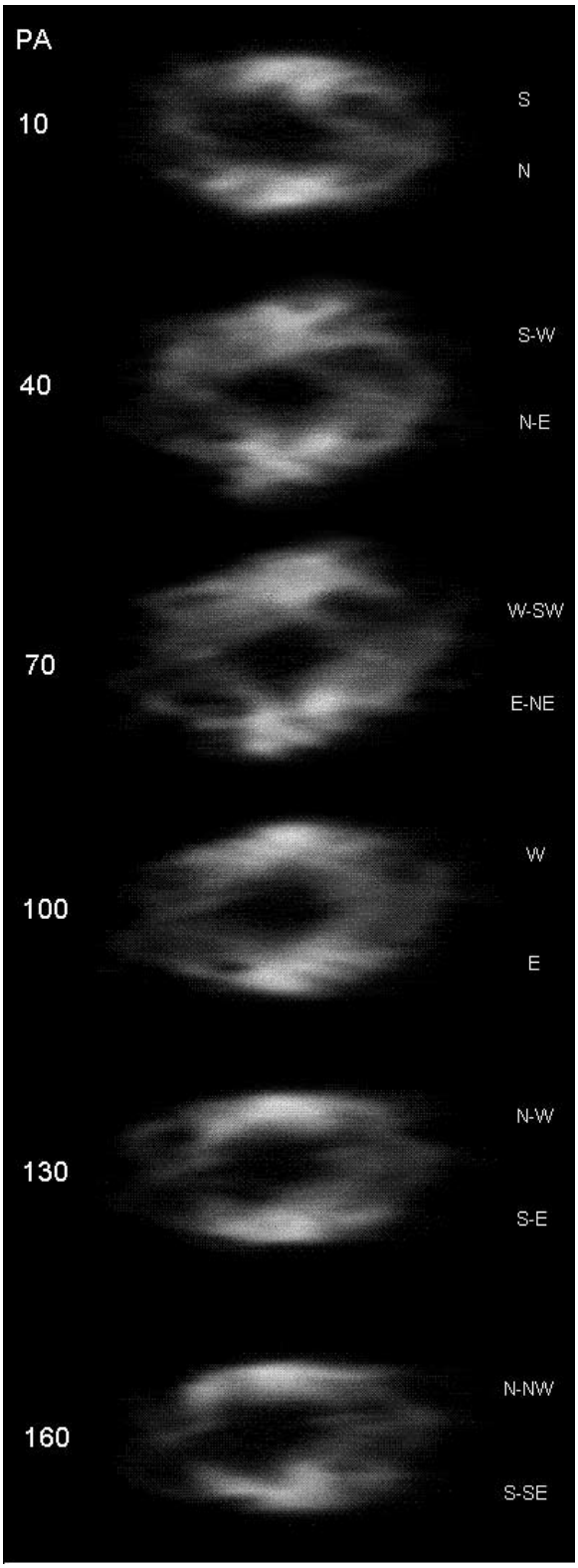

FIG. 6.—Combined position-velocity maps of NGC 6720 at six selected P.A.'s in high- (He II), medium- ([O III]), and low-ionization ([N II]) zones, scaled according to the relation $V_{\rm exp}(\text{km s}^{-1}) = 0.65R''$. The orientation of these tomographic maps is the same as in Fig. 2. [*See the electronic edition of the Journal for a color version of this figure*.]

[8] The physical justification for the adopted value r''(poles) $\simeq 1.5r''$(major axis of the equator) is presented in § 6.3.

[9] Guerrero et al. (1997) find $i \simeq 30^\circ$ by fitting the line tilt and the apparent nebular morphology with a uniform prolate ellipsoidal (sic) shell expanding with $V_{\rm exp} \propto R$.

[10] See http://web.oapd.inaf.it/sabbadin.

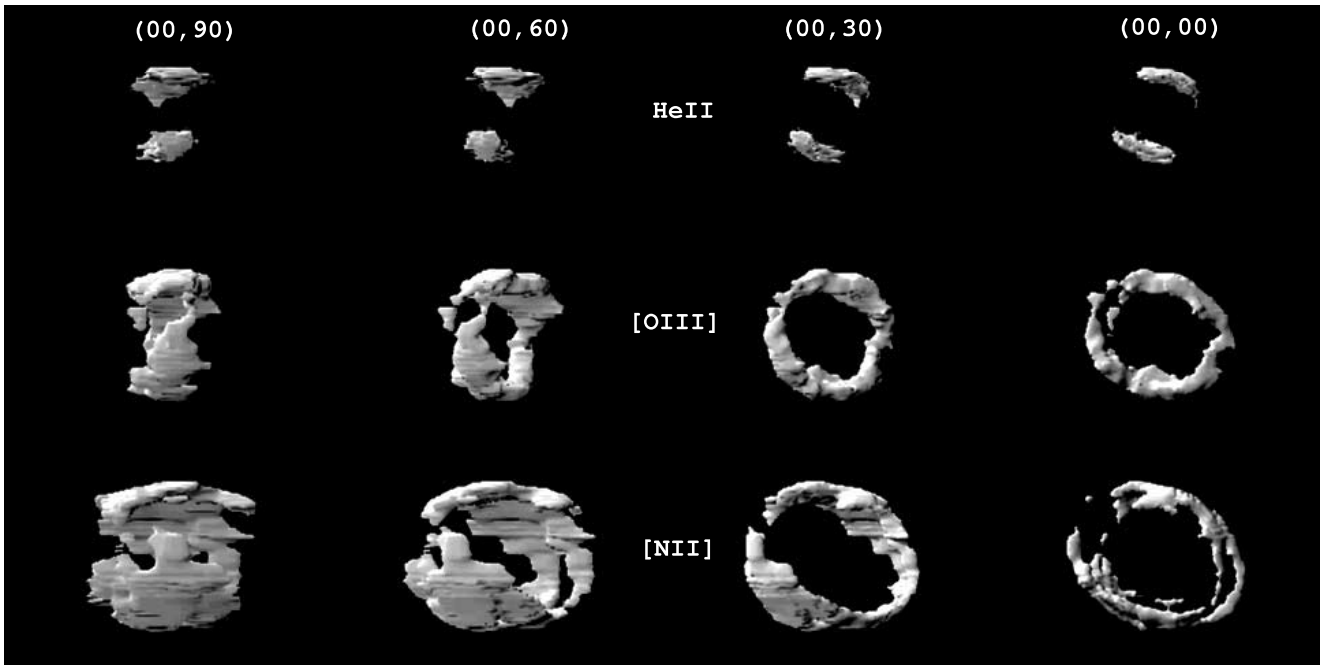

FIG. 7.—Opaque reconstruction of NGC 6720 at high flux levels (i.e., the brightest regions) in He II (*top row*), [O III] (*middle row*), and [N II] (*bottom row*), as seen from four directions separated by 30° and covering a right angle. The line of sight is given by (θ, ψ), where θ is the zenith angle and ψ the azimuthal angle. The (00, 00) images represent the rebuilt nebula as seen from the Earth (north is up, and east to the left). [*This figure is available as part of an mpeg animation with Fig. 10 in the electronic edition of the Journal.*]

levels for a rotation of 90° through the first Euler angle. The (00,00) images correspond to the Earth-nebula direction (north is up, and east to the left).

The Ring Nebula appears as an open-ended, almost prolate ellipsoid at high ionization (He II), as a close triaxial ellipsoid at mean ionization ([O III]; the same occurring in the Hα reconstruction, not presented here), and as an open-ended triaxial ellipsoid at low ionization ([N II]).

The long linear features in the line-of-sight direction (for example, in the (00,90) projection of [N II] in Fig. 9) are a consequence of the limited "relative spectral resolution" (which is much lower that the "relative spatial resolution") of our echellgrams.

The transparent projection of NGC 6720 for a rotation around the north-south direction is presented in Figure 10 (multicolor images in the electronic version). It provides a representative sample of the apparent morphology when changing the line of sight. Figure 10 (*left*) corresponds to Figure 3 (*bottom right*) and represents the Ring Nebula as seen from the Earth (i.e., nearly pole-on). The excellent agreement of the results of this analysis and the optical appearance of the nebula argue that the linear expansion law is closely followed for NGC 6720. The optical appearance of NGC 6720 seen from (00,00) recalls NGC 6781 and NGC 2438; from (00,30) it resembles NGC 7293 and NGC 6563; and from (00,90) it looks like IC 4406. All of these objects are extended, evolved PNe in the same evolutionary phase as NGC 6720. Moreover, the Ring Nebula seen from (00,00) mimics SP 1, a pole-on, high-excitation PN with a binary central star (Bond & Livio 1990; Mitchell et al. 2006).

Figures 7–10 confirm our earlier conclusion that NGC 6720 is a triaxial ellipsoid (axial radii of 0.10, 0.13, and 0.20 pc) seen nearly pole-on and denser in the optically thick equatorial regions than at the optically thin poles. Triaxiality appears as a common

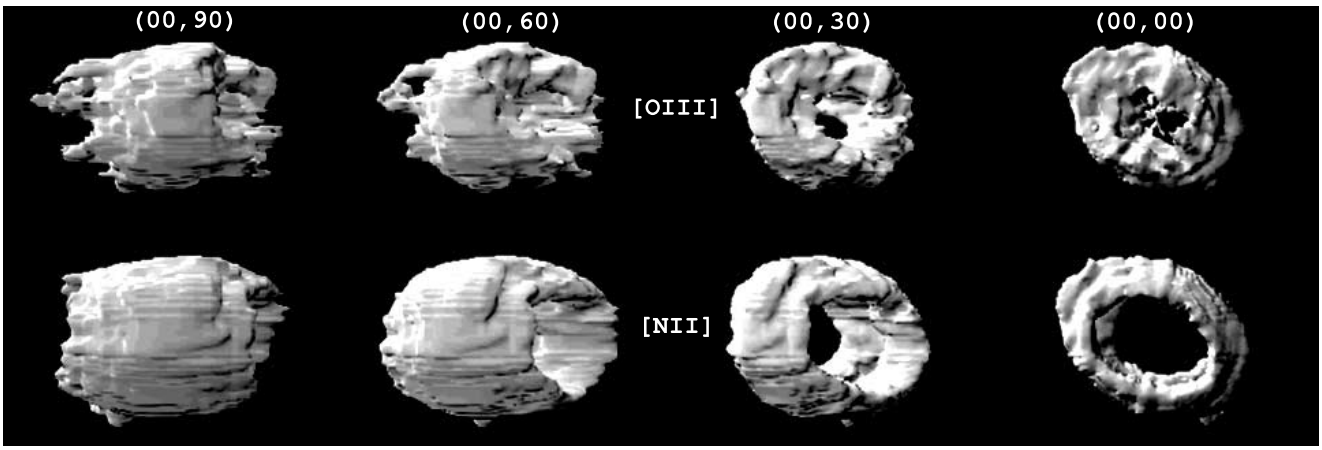

FIG. 8.—Opaque reconstruction of NGC 6720 in [O III] and [N II] at the mean flux levels. Same orientation as Fig. 7.

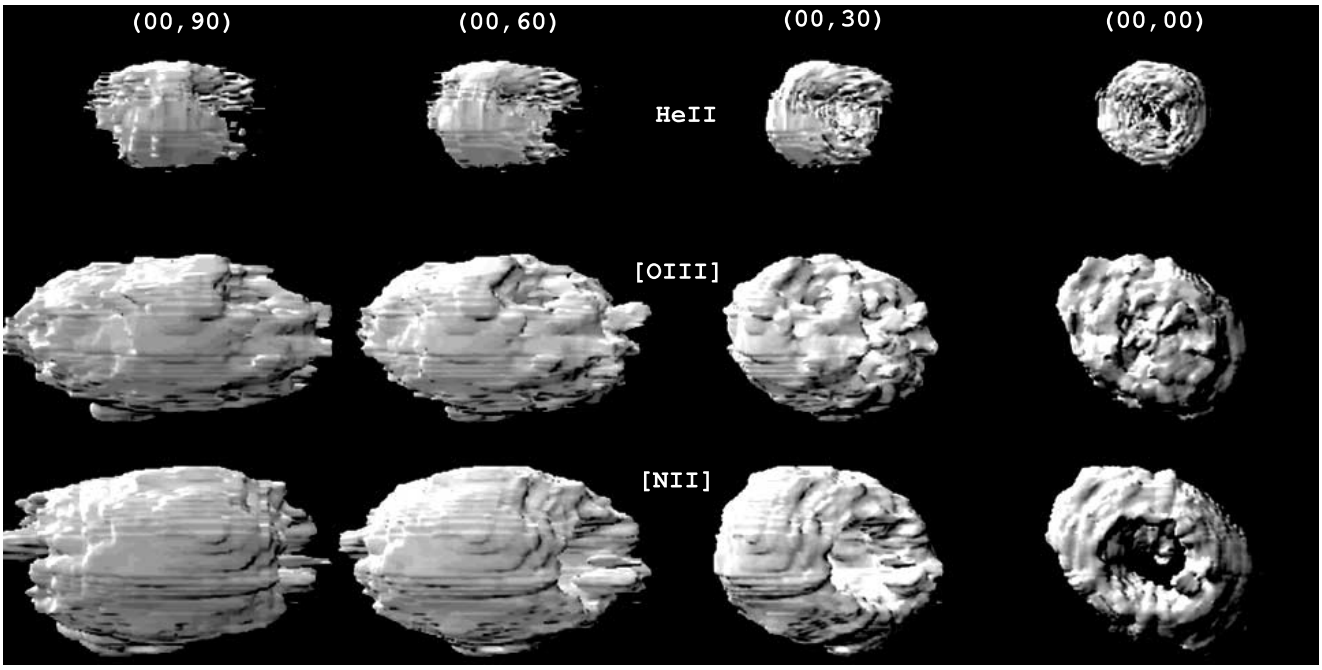

FIG. 9.—Opaque reconstruction of NGC 6720 in He II, [O III], and [N II] at low flux levels (i.e., the faintest regions). Same orientation as Figs. 7 and 8.

characteristic of the PNe studied by the Paduan team, e.g., NGC 1501 (Ragazzoni et al. 2001), NGC 6565 (Turatto et al. 2002), NGC 6818 (Benetti et al. 2003), NGC 7009 (Sabbadin et al. 2004), and NGC 6741 (Sabbadin et al. 2005).

5. THE IONIZATION AND DENSITY STRUCTURE OF THE RING NEBULA

Knowledge of both the distance and the spatio-kinematical properties of an expanding nebula allows us (Sabbadin et al. 2006) to use the extinction-corrected fluxes to quantify the pixel-to-pixel absolute emissivity in the different lines, and the radial $N_e\epsilon_l^{0.5}$ profile from Hα (where ϵ_l is the local filling factor; i.e., the fraction of the local volume actually filled by matter with density N_e). The resulting $N_e\epsilon_l^{0.5}$ distributions for the minor axis of the equator, the major axis of the equator, and the poles of NGC 6720 are shown in the top panels of Figures 11, 12, and 13, respectively (we have assumed a constant value of $T_e = 10^4$ K). The lower panels of Figures 11–13 contain the corresponding absolute emissivity profiles (ergs cm^{-3} s^{-1}) of the different emissions.

In the equatorial regions of NGC 6720 (Figs. 11 and 12), $N_e\epsilon_l^{0.5}$ monotonically increases outward up to a peak of about 650–750 cm^{-3} (minor axis) and 450–550 cm^{-3} (major axis). It is likely that the fall of the electron density in the external regions and the enhancement of low-ionization species are due to the presence of an ionization front (i.e., in these directions the nebula is optically thick to LyC from the central star).

Although the $N_e\epsilon_l^{0.5}$ polar profile of the Ring Nebula (Fig. 13) is less accurate than the equatorial profile (because of the limited relative spectral resolution of our spectra: $SS = V_{\rm exp}/\Delta V \simeq 5$), it demonstrates an $N_e\epsilon_l^{0.5}$ peak of 200–250 cm^{-3}, confirming the results of § 4.1. Moreover, the absolute flux distribution in the different lines confirms that the high-latitude regions are optically thin to the LyC radiation.

The $N_e\epsilon_l^{0.5}$ profiles obtained from the absolute Hα flux can be compared with the N_e measurements reported in the literature derived from line intensity ratios of ions in the p^3 configuration (mainly the 6717 and 6731 Å lines of [S II]). These yield $N_e \simeq$ 600–800 cm^{-3} for the brightest regions of the projected image of NGC 6720 (Hawley & Miller 1977; Barker 1987; Guerrero et al. 1997; Liu et al. 2004; Wang et al. 2004). Thus, in the following we adopt $\epsilon_l = 1$.

The ionized mass can be obtained in different ways: from the observed N_e spatial distribution, the Hβ flux, and the radio flux (Aller 1984; Pottasch 1984; Osterbrock 1989; Turatto et al. 2002). We derive $M_{\rm ion} \simeq 0.06 \pm 0.02\ M_\odot$, but it is important to note that this is only a fraction of the total mass, since NGC 6720 is ionization-bounded along the equator.

The existence of neutral gas surrounding the equatorial regions of NGC 6720 is established by the radial ionization structure (Figs. 11 and 12). In addition, there is clumpy structure of atomic and molecular emission (Kastner et al. 1994; Speck et al. 2003; Hiriart 2004; and references therein) and an irregular series

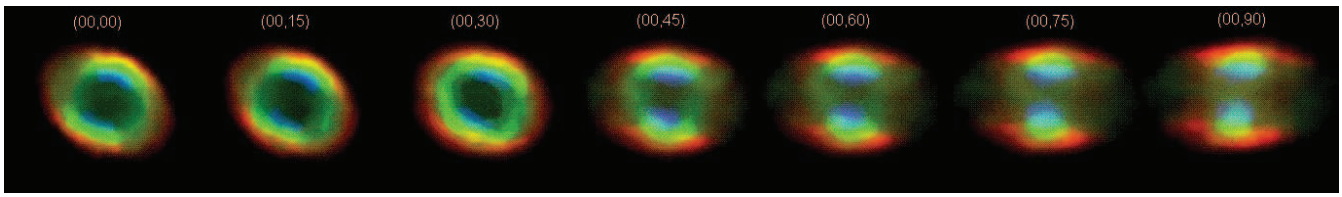

FIG. 10.—Optical appearance of NGC 6720 (He II, *blue*; [O III], *green*; [N II], *red*) for a rotation through the north-south axis centered on the exciting star. The leftmost panel, (00, 00), corresponds to the rebuilt nebula as seen from the Earth (north is up, and east to the left). [*This figure is available as part of an mpeg animation with Fig. 7 in the electronic edition of the Journal.*]

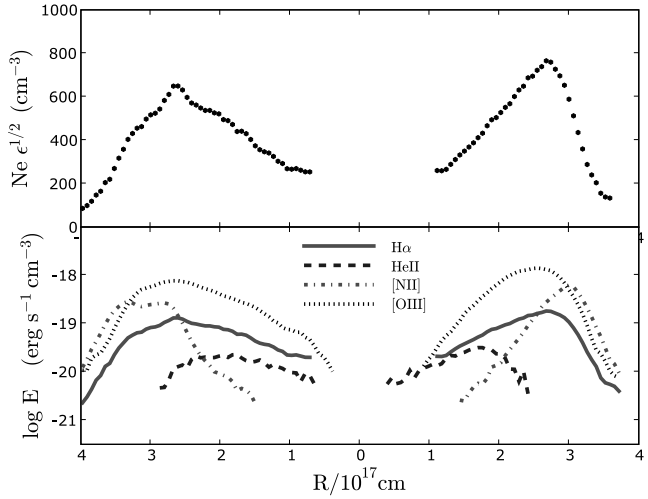

FIG. 11.—Nebular characteristics of NGC 6720 along the entire minor axis of the elliptical equator (the zvpc at P.A. = 160°; see Fig. 4, *top*). *Top*: Radial $N_e\epsilon_l^{0.5}$ profile (ϵ_l is the local filling factor) from the absolute Hα flux (assuming $T_e = 10^4$ K). *Bottom*: Absolute emissivity profile (ergs cm^{-3} s^{-1}) in the different emissions. The south-southeast sector is at the left, and the north-northwest at the right. The central star position is at $X = 0$. [*See the electronic edition of the Journal for a color version of this figure.*]

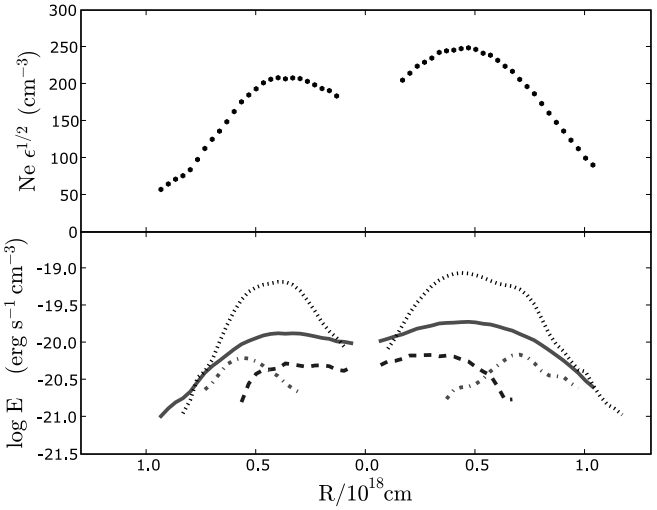

FIG. 13.—Nebular characteristics of NGC 6720 along the entire polar axis (cspl; see Fig. 5). *Top*: Radial $N_e\epsilon_l^{0.5}$ profile from the absolute Hα flux (for $T_e = 10^4$ K). *Bottom*: Absolute emissivity profile (ergs cm^{-3} s^{-1}) in the different emission lines. The central star position is at $X = 0$. Approaching gas is to the left. Symbols are the same as Figs. 11 and 12. [*See the electronic edition of the Journal for a color version of this figure.*]

of dark knots in the *HST* images which are more evident in Hα and [O III].

Information on the properties of the knots seen in silhouette against the main nebula can be obtained from the optical depth in [O III]. This extinction is due to scattering and absorption in grains within the knots. We have used the *HST* images to derive several intensity scans in the neighborhood of the deepest knots of NGC 6720, obtaining a contrast ratio up to 2.2 ± 0.2, i.e., a $c_{H\beta}$(knot) up to 0.35 ± 0.05. For a "normal" gas-to-dust ratio (Spitzer 1978; Bohlin et al. 1978), $c_{H\beta} = 1.48E(B-V)$ (Acker 1978), and a radial thickness of the absorbing knot comparable with the apparent diameter, we derive a characteristic value of the H I density of $N(\text{H I}) \simeq (1.0 \pm 0.2) \times 10^4$ atoms cm^{-3}. Such a high density in the knots of NGC 6720 is similar to that of other recombining or reionizing PNe studied in detail, namely, IC 4406, NGC 6853, and NGC 7293 (O'Dell et al. 2002), NGC 6565 (Turatto et al. 2002), NGC 6818 (Benetti et al. 2003), and NGC 6741 (Sabbadin et al. 2005).

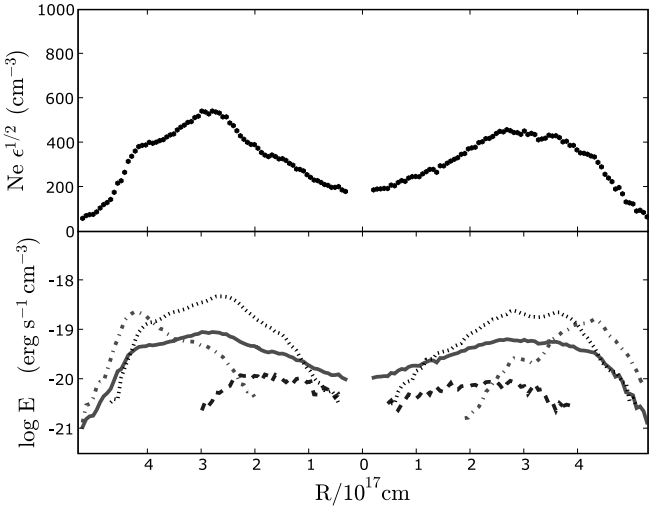

FIG. 12.—Nebular characteristics of NGC 6720 along the entire major axis of the elliptical equator (zvpc at P.A. = 70°; see Fig. 4, *bottom*). *Top*: Radial $N_e\epsilon_l^{0.5}$ profile from the absolute Hα flux (for $T_e = 10^4$ K). *Bottom*: Absolute flux profile (ergs cm^{-3} s^{-1}) in the different emissions. The east-northeast sector is at the left, and the west-southwest at the right. The central star position is at $X = 0$. Same symbols as Fig. 11. [*See the electronic edition of the Journal for a color version of this figure.*]

6. DISCUSSION

Our new information about NGC 6720 can be used to derive additional characteristics of this object and to fit that information into the broader base of knowledge about PNe. In § 6.1 we use the present conditions of the central star and the nebula to derive the ionization history of NGC 6720. In § 6.2 we compare the observed radial ionization structure of the nebula with results predicted by the Cloudy ionization code. The limits of our spatio-kinematical reconstruction and a comparison with the best theoretical models are discussed in § 6.3, while the similarities of NGC 6720 and NGC 7293 are described in § 6.4. The observed properties of the knots within NGC 6720 and other PNe are compared with theoretical predictions in § 6.5, while our results are summarized in § 6.6.

6.1. *The Derived Characteristics of the Central Star and the Ionization History of NGC 6720*

Knowing the characteristics of the central star and the current conditions within the nebula, we can use the well-defined theory of the evolution of the central stars of PNe to explain the nebula's recent past and imminent future. One can derive the age for NGC 6720 from its distance and expansion scale factor. With our adopted distance of 700 pc and expansion relation $V_{\text{exp}}(\text{km s}^{-1}) = 0.65R''$, the "kinematic" age, $t_{\text{kin}} = R/V_{\text{exp}}$, is about 5200 yr, whereas the "true" age (which assumes that the starting velocity of the newborn PN is that of the AGB wind)

$$t_{\text{true}} \simeq 2R/\left[V_{\text{exp}}(\text{today}) + V_{\text{exp}}(\text{AGB})\right] \simeq 7000 \text{ yr}$$

[for $V_{\text{exp}}(\text{AGB}) = 15$ km s^{-1}].[11]

[11] O'Dell et al. (2002) used *HST* WFPC2 images over an interval of 2 years to argue that the ionized nebula is expanding in the plane of the sky with a timescale of about 1500 yr. However, it is likely that their stated probable error of 15% is much more uncertain, as they neglected the long-term drift in relative position of the four CCDs (Anderson & King 2003).

The stellar characteristics from § 1.3 ($\log L/L_\odot = 2.3 \pm 0.2$, $\log T \simeq 5.10 \pm 0.02$) and the nebular age of NGC 6720, together with Blöcker's (1995) theoretical post-AGB evolutionary tracks, allow us to infer the stellar mass, $M_* \simeq 0.61$–$0.62\ M_\odot$, i.e., slightly larger than the average value of the PNe nuclei of $\simeq 0.60\ M_\odot$ (Schönberner 1983; Vassiliadis & Wood 1993; Blöcker 1995). This conclusion is not very sensitive to the errors we assign to the stellar temperature and luminosity. Knowing these present characteristics and the theoretical stellar evolution tracks, we can trace the evolution of the ionization of the nebula.

The star has recently (about one to two thousand years ago) exhausted hydrogen-shell nuclear burning, and is approaching the white dwarf cooling sequence. The early luminosity decline would have been very fast, causing the ionization front to stop advancing and probably to even retreat in the dense equatorial region. Later, as the drop in LyC luminosity (Q) slowed, this expanding gas would have passed the stage of ionization boundary contraction-expansion equilibrium, $(1/3)(d \ln Q/dt) = -1/t_{\rm kin}$, for a classical Strömgren sphere, and the current phase of the expanding ionization front (late-phase PN) would have started. However, the low-density polar regions of the main nebula would remain fully ionized during the star's luminosity decline.

Our scenario for the evolution accounts for the double-structure appearance of the external, faint halos of NGC 6720 (mentioned in § 1.1). The inner, brighter, and elongated halo represents the pole-on projection of the AGB wind at high latitudes (i.e., circumpolar) directly ionized by the present UV flux of the low-luminosity central star. This is allowed because the main nebula is optically thin in the polar directions. The outer, fainter, and circular halo is the projection of the recombining AGB wind at mean to low latitudes. This gas was ionized by the UV flux in the past high-luminosity phase of the hot central star when direct and scattered (recombination) LyC photons would have illuminated the entire outer region. This model disentangles the true, intrinsic nature of the halos surrounding NGC 6720, accounts for the elongated appearance of the inner halo (it mimics the elliptical equator of the main nebula), agrees with the chemical and kinematical results by Guerrero et al. (1997), and can be applied to the double halo of other recombining PNe seen pole-on (for example, NGC 2438; see Corradi et al. 2000). Both of the NGC 6720 halos are very similar in images taken in the [O I] λ6300 line (Lame & Pogge 1994) and the H_2 2.12 μm line (Kastner et al. 1994). Since the H_2 emission must come from a narrow region of a PDR (O'Dell et al. 2007), this is a strong argument that both of these halos are now ionization-bounded.

6.2. *Applying the Photoionization Model Cloudy to the Ring Nebula*

We have applied the photoionization code Cloudy[12] to a model nebula characterized by the same distance (700 pc), mean chemical composition (taken from the literature), and similar exciting star parameters ($\log L/L_\odot = 2.3$, $\log T = 5.10$) as NGC 6720. We did this calculation for gas distributions characteristic of three primary vectors in NGC 6720, namely,

1. The matter profile along the semiminor axis of the elliptical equatorial belt. We selected the north-northwest sector of the zvpc in P.A. $= 160^\circ$ (right part of Fig. 11, *top*);

2. The matter profile along the semimajor axis of the elliptical equatorial belt. We selected the west-southwest sector of the zvpc in P.A. $= 70^\circ$ (right part of Fig. 12, *top*);

[12] Calculations were performed with version 05.07b of the spectral simulation code Cloudy, last described by Ferland et al. (1998).

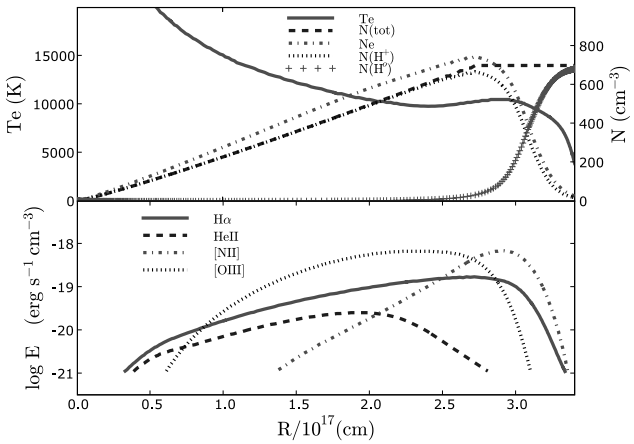

FIG. 14.—Application of the photoionization code Cloudy to the semiminor axis of the elliptical equator of NGC 6720 (north-northwest sector of the zvpc in P.A. $= 160^\circ$), to be compared with the right plots of Fig. 11. *Top*, Physical conditions; *bottom*, absolute line fluxes. [*See the electronic edition of the Journal for a color version of this figure*.]

3. The density profile of the approaching matter along the polar axis (left part of Fig. 13, *top*).

There is an important caveat to this application of Cloudy, since it applies to steady state nebulae in ionization and thermal equilibrium, whereas we have previously inferred (§ 6.1) that in the recent past (about one to two thousand years ago) the central star of NGC 6720 underwent a quick luminosity drop followed by a progressively slower decline. The effects of this ionizing flux variation would have been different for the equatorial and the polar nebular regions. The recombination time for hydrogen, $t_{\rm rec} \simeq 120{,}000/N_e$, is 150–200 yr for the dense equator of NGC 6720, and longer than 500 yr for the polar regions. Given the recombination timescales and the timescale of change of the central star, we can consider the Ring Nebula "nearly" in equilibrium and apply the steady state photoionization code Cloudy to the three selected radial density profiles (this being satisfactory for the equatorial profiles but with some limitations for the polar direction, as the polar regions reflect conditions of gas recombining from an earlier, higher ionization stage).

The results for the model nebula are contained in Figures 14–16, showing the physical conditions (*top panels*) and the absolute flux distributions of the main emission lines (*bottom panels*). Comparison of these emission-line profiles with the corresponding trends observed in the Ring Nebula (Figs. 11–13) indicates very satisfactory agreement along the minor and the major semiaxes of the equator (confirming that these regions are ionization-bounded) but inadequate agreement for the polar regions. The disagreement at the poles occurs because the limited spectral resolution of the spectra can only provide a rough radial density profile along the poles of the Ring Nebula (from the cspl), and the recombination time of these diluted, optically thin regions is comparable to the time elapsed since the central star's drop in LyC luminosity.

6.3. *Critical Comparison of the Spatio-kinematical Recovered and Theoretical Models*

The reionizing Ring Nebula follows Wilson's law of homologous expansion, at least to the level that ions of progressively higher ionization expand more slowly, as commonly observed in this class of objects. Wilson's law is in general agreement with the kinematics of late-stage PNe models with a higher mass central star coming from updated radiation-hydrodynamic simulations

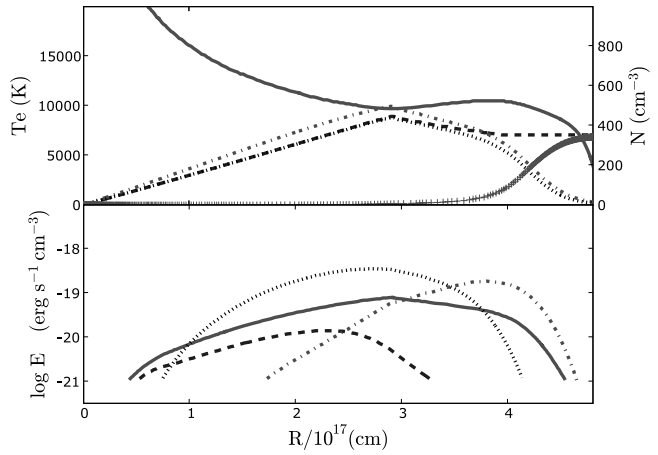

FIG. 15.—Application of the photoionization code Cloudy to the semimajor axis of the elliptical equator of NGC 6720 (west-southwest sector of the zvpc in P.A. = 70°), to be compared with the right plots of Fig. 11. *Top*, Physical conditions; *bottom*, absolute line fluxes. Same symbols as Fig. 14. [*See the electronic edition of the Journal for a color version of this figure*.]

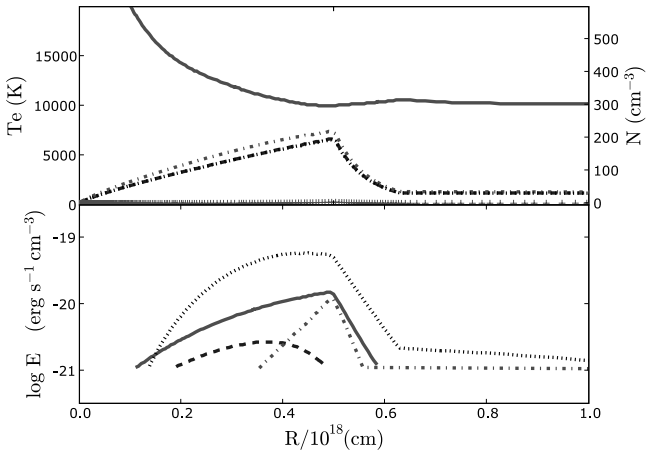

FIG. 16.—Application of the photoionization code Cloudy to the polar radius of NGC 6720 (approaching gas in the cspl), to be compared with the left plots of Fig. 12. *Top*, Physical conditions; *bottom*, absolute line fluxes. Same symbols as Figs. 14 and 15. [*See the electronic edition of the Journal for a color version of this figure*.]

(Perinotto et al. 2004 and references therein). However, these models have a large central cavity, whereas the Ring Nebula's core is filled with highly ionized gas. Moreover, radiation-hydrodynamic models for PNe in an earlier evolutionary phase show a "reversed Wilson's law." These discrepancies call for severe constraints on the evolutionary parameters responsible for PNe shaping, including the wind interaction. The accelerating effects of the high-velocity wind on the innermost nebular layers clash with Wilson's finding of the lowest expansion velocities in the high-ionization [Ne V] zone (Wilson 1950).

The true kinematics of a complex object like a PN is more complex than the simple Wilson's law, as it must include different expansion laws for the inner and the outer envelopes, possible localized transverse motions, shocks, turbulence, fine-scale flows due to local pressure gradients, and effects that we do not now envision. These conditions also apply to NGC 6720, with the aggravating circumstance that it is seen nearly pole-on. Such a peculiar angle of view forces us (see § 4.1) to arbitrarily adopt the polar ellipticity ratio

$$P = R''(\text{poles})/R''(\text{major axis of the equator}) = 1.5,$$

which leads to $A = 0.65$ km s^{-1} arcsec^{-1} and the spatial reconstruction shown in Figures 7–10. However, this value of P is probably the most likely value. In fact, $P = 1.5$ is the lowest allowable value since smaller values imply $\epsilon_1 > l$ (Sabbadin et al. 2006), which is unphysical. On the other hand, values of $P > 1.5$ would imply unrealistic kinematical properties for the main nebula, that is, $V_{\rm exp}(\text{equator}) \propto P^{-1}$ (see § 4.1). For example, $P \geq 2.0$ gives $V_{\rm exp}(\text{equatorial minor axis}) \leq 15$ km s^{-1}, i.e., as low as (or even lower than) $V_{\rm exp}$(AGB).

In summary, the spatio-kinematical results presented in this paper furnish a detailed, self-consistent, large-scale reconstruction of the Ring Nebula. It requires refinement by means of multi-P.A. spectra at higher spatial and spectral resolutions.

6.4. *The Similarities of the Ring Nebula and the Helix Nebula*

As the closest bright PN, the Helix Nebula (NGC 7293, PNG 036.1−57.1; Acker et al. 1992) offers the potential of study in much greater detail than in other PNe; however, its low surface brightness presents an observational problem, which has limited the number of studies. Although well studied through imaging, its velocities have not been thoroughly mapped, and the resulting kinematical age lies in the broad range of 6560 yr (O'Dell et al. 2004) to about 22,000 yr (Meaburn et al. 2005), depending on the adopted spatio-kinematical model.

According to O'Dell et al. (2004), the inner structure of NGC 7293 is an ionization-bounded toroidal disk ($d = 499''$) expanding at 40 km s^{-1}, with an extended, bipolar vertical component and an axis tilted 28° from the line of sight. It is surrounded by a nearly perpendicular incomplete ring ($d = 742''$, $V_{\rm exp} = 32$ km s^{-1}) inclined 53° to the plane of the sky, and by an outermost ring ($d = 1500''$) flattened by collision with the ambient interstellar medium.

Meaburn et al. (2005) infer that the inner structure of the Helix Nebula is a spherical, slowly expanding shell ($d = 300''$, $V_{\rm exp} \simeq 12$ km s^{-1}) surrounded by a bipolar nebula consisting of a central toroid ($d = 600''$) expanding at 14.25 km s^{-1} and of two polar lobes (major axis of 980″ tilted 37° to the line of sight) with $V_{\rm exp} = 24.5$ km s^{-1}.

There is a remarkable similarity of appearance between the Ring and Helix Nebulae, but there are important differences in their physical characteristics. The Helix Nebula is larger (central disk diameter of 0.26 pc as compared to the Ring Nebula's 0.10 pc) and less dense (central disk peak densities of about 60 and 600 cm^{-3}, respectively). The Helix Nebula's He II central core as defined by its He II λ4686 emission is concentrated toward the direction of the central star (O'Dell 1998) and is expanding with a velocity of about 9 km s^{-1} (O'Dell 2005), whereas the Ring Nebula's central core is expanding at about 19 km s^{-1}, and there is evidence from both images and the dynamics that it is an expanding shell. The Helix Nebula has an accurate trigonometric parallax (Harris et al. 2007), and its central star's spectrum and brightness have been well studied (Bohlin et al. 1982), yielding a luminosity of $112^{+29}_{-20}\,L_\odot$ and $T_{\rm eff} = 123{,}000$ K (O'Dell & Burkert 1997). Like the Ring Nebula's central star, there is no spectroscopic evidence of a stellar wind in the central star of the Helix Nebula (Cerruti-Sola & Perinotto 1985).

Comparison with the theoretical evolution models of Blöcker (1995) indicates that the Helix Nebula's star is of a similar mass but is more evolved than that of the Ring Nebula. The Helix Nebula is an older object, as indicated by size, density, kinematic age, and the central star characteristics. It is essentially an "older twin" of the Ring Nebula.

It is likely that the different velocity and density distributions in the He II core reflect the fact that the Helix Nebula has had a longer time to readjust its inner structure after the cessation of the high-velocity stellar wind phase. Without the sustaining outward forces that originate from the high-velocity stellar wind, it must be inevitable that a certain back-filling of material occurs, giving a different density distribution and lower effective expansion velocity. We are not aware of nebula evolution models that treat this phase in adequate detail.

6.5. *The Ring, the Helix, and Other "Knotty" Planetary Nebulae*

We have established that for NGC 6720 the second expansion of the ionization front has occurred recently, while in the "older twin" NGC 7293 this occurred several thousand years ago, so that the knots (sculpted into cometary forms) are distributed from the reionization front to well inside the ionized zone (although not as far in as the He II core; O'Dell et al. 2007). These two well-studied nebulae are useful in understanding the evolution of the knots detected in several nearby PNe (O'Dell et al. 2002; Sabbadin et al. 2005; and references therein) and in disentangling the different theoretical explanations advanced for their production (Capriotti 1973; Vishniac 1994; Williams 1999; García-Segura et al. 1999, 2006; Steffen & López 2004; and references therein).

The nebulae in which knots are observed are the more evolved objects, with lower luminosity central stars. In most cases, the knots are found approximately at the ionization front or interior to it. In addition to the well-observed knots in the Ring and Helix Nebulae, a system of obscuring features and knots are found in the *HST* images of the recombined PNe II 4406, NGC 6853, and NGC 3132 (O'Dell et al. 2002), NGC 6565 (Turatto et al. 2002), NGC 6818 (Benetti et al. 2003), and NGC 6741 (Sabbadin et al. 2005). The distance to these objects is between 0.7 and 2.0 kpc, establishing that *HST* imaging allows the detection of occulting (or emitting) knots in relative distant nebulae.

Similar features are not observed in *HST* images of pre–recombined stage mean- to high-ionization PNe powered by a hot and high-luminosity star, e.g., NGC 1535, NGC 2022, NGC 2610, NGC 2792, NGC 3242, NGC 3918, NGC 4361, NGC 6153, NGC 7008, NGC 7009, and NGC 7662.[13]

These systematic differences suggest that knot formation is related to dynamical instabilities at the ionization front of recombined and late-stage PNe powered by a massive, fast evolving central star. According to García-Segura et al. (1999), "...in regions where the ionization front is not trapped at all, the shells are much smoother and thicker because of the uniform thermal pressure. In regions where the ionization front is marginally trapped, vigorous dynamical instabilities develop."

There is a pressing need for a thorough study (both theoretical and observational) that extends to a large sample of PNe in different evolutionary phases. Since the knots in PNe are known to be bright in H_2 emission (NGC 7293: O'Dell et al. 2002 and references therein; NGC 6720: Speck et al. 2003, Hiriart 2004; NGC 6853: McCandliss et al. 2007), these molecules are indicators that the knot material is at least in part formed from material that has not recently been ionized. If the presence of H_2 in knots is a general phenomenon, then this becomes an important constraint on the formation of knots. Knots could not be forming in PNe that have recently undergone complete ionization and would be possible only in those PNe where the expansion of the initial ionization front stopped prior to reaching a density-bounded condition.

A striking case that contrasts with typical PNe is the PN NGC 2392 (the Eskimo Nebula, PNG 197.8+17.3; Acker et al. 1992), where an inner, high-ionization disk rich in loops and filaments is surrounded by a bright crown of low-ionization cometary knots within an outer envelope (O'Dell et al. 2002). This "strangeness," added to other observational peculiarities (i.e., gas kinematics and the central star's properties; O'Dell et al. 1990; Pauldrach et al. 2004), suggests that the Eskimo Nebula could be a "born-again" PN. In this scenario, the PN evolution regularly proceeds until the star has declined in luminosity and a system of absorbing knots has grown in the external, recombining layers of the main nebula. During the slow stellar motion toward the white dwarf domain, a late thermal pulse expels new photospheric material and brings the star back to the low-temperature and high-luminosity zone of the H-R diagram. The star restarts its evolution toward higher temperatures, and in a few thousand years an NGC 2392–like nebula appears.

6.6. *Summary of Our Results*

We have successfully constructed a 3D model of the Ring Nebula using high-resolution spectra. The nebula shows the homologous expansion common to many PNe. It is a triaxial ellipsoid with its smaller axes lying almost in the plane of the sky and with a greater density concentration in this equatorial plane, which is ionization bounded, whereas the polar axes are optically thin to LyC photons.

The PN, about 7000 yr old, is in what we call the late phase for PNe, when the luminosity-fading timescale of the central star has exceeded the expansion timescale of the nebula. Like a number of other recombined and late-phase PNe, we find that multiple concentrations (knots) have formed near the equatorial ionization boundary and may have been established by dynamical instabilities at the ionization front. In any event, the knots appear to have formed during or after reaching the recombined phase or the late phase, rather than in earlier phases when the ionization front was first growing. The oval inner halo of NGC 6720 is ionized by LyC photons escaping through the poles of the main nebula, while the larger spherical outer envelope shines by fossil emission from the early, more luminous phase of the central star. The Ring Nebula is essentially a younger twin of the larger Helix Nebula, and like that nebula a high-ionization zone of gas occupies the center, in contrast with the predictions of even the best hydrodynamic models of PNe.

We must acknowledge the important role of the late Donald E. Osterbrock in defining the astrophysics of gaseous nebulae. His fundamental work has allowed us to address the structure and evolution of PNe and many other subjects. Without his efforts, this work could not have been done. The analysis program for deriving a 3D model of a PN from maps of its radial velocity was developed as a joint effort of Stefano Benetti, Enrico Cappellaro, Roberto Ragazzoni, and Massimo Turatto of INAF-Astronomical Observatory of Padua, Italy. We are grateful to these colleagues for allowing the use of their analysis program for this project. Massimo Turatto kindly contributed to the preparation of this manuscript. Guillermo García-Segura provided important information supplementing his recent paper about the formation of the knots. Part of C. R. O.'s support for work on this project came from grant GO 10628 from the Space Telescope Science Institute. W. J. H. acknowledges financial support from DGAPA-UNAM, Mexico, project IN112006.

[13] The so-called SLOWERs and FLIERs of NGC 7662 are normal regions of the outer envelope (same density, kinematics, and chemical abundances), simply shadowed by the main rim. The same consideration applies to the ansae and the caps of NGC 7009. More details are in Sabbadin et al. (2005, 2006).

REFERENCES

Acker, A. 1978, A&AS, 33, 367
Acker, A., Marcout, J., Ochsenbein, F., Stenholm, B., & Tylenda, R. 1992, Strasbourg-ESO Catalog of Galactic Planetary Nebulae (Garching: ESO)
Aller, L. H. 1984, Physics of Gaseous Nebulae (Dordrecht: Kluwer)
Aller, L. H., Epps, H. W., & Czyzak, S. J. 1976, ApJ, 205, 798
Anderson, J., & King, I. R. 2003, PASP, 115, 113
Atherton, P. D., Hicks, T. R., Reay, N. K., Worswick, S. P., & Smith, W. H. 1978, A&A, 66, 297
Barker, T. 1987, ApJ, 322, 922
Benetti, S., Cappellaro, E., Ragazzoni, R., Sabbadin, F., & Turatto, M. 2003, A&A, 400, 161
Blöcker, T. 1995, A&A, 299, 755
———. 2001, Ap&SS, 275, 1
Bohlin, R. C., Harrington, J. P., & Stecher, T. P. 1982, ApJ, 252, 635
Bohlin, R. C., Savage, B. D., & Drake, J. F. 1978, ApJ, 224, 132
Bond, H. E., & Livio, M. 1990, ApJ, 355, 568
Bryce, M., Balick, B., & Meaburn, J. 1994, MNRAS, 266, 721
Capriotti, E. R. 1973, ApJ, 179, 495
Cerruti-Sola, M., & Perinotto, M. 1985, ApJ, 291, 237
Clegg, R. E. S., Miller, S., Storey, P. J., & Kisielius, R. 1999, A&AS, 135, 359
Corradi, R. L. M., Schönberner, D., Steffen, M., & Perinotto, M. 2000, A&A, 354, 1071
Esteban, C., Peimbert, M., Torres-Peimbert, S., & Escalante, V. 1998, MNRAS, 295, 401
Ferland, G. J., Korista, K. T., Verner, D. A., Ferguson, J. W., Kingdon, J. B., & Verner, E. M. 1998, PASP, 110, 761
García-Segura, G., Langer, N., Różyczka, M., & Franco, J. 1999, ApJ, 517, 767
García-Segura, G., López, J. A., Steffen, W., Meaburn, J., & Manchado, A. 2006, ApJ, 646, 61
Garnett, D. R., & Dinerstein, H. L. 2001, ApJ, 558, 145
Guerrero, M. A., Manchado, A., & Chu, Y.-H. 1997, ApJ, 487, 328
Harris, H. C., et al. 2007, AJ, 133, 631
Hawley, S. A., & Miller, J. S. 1977, ApJ, 212, 94
Herwig, F., Blöcker, T., Langer, N., & Driebe, T. 1999, A&A, 349, L5
Hiriart, D. 2004, PASP, 116, 1135
Kaler, J. B. 1983, ApJ, 271, 188
Kaler, J. B., & Jacoby, G. H. 1989, ApJ, 345, 871
Kastner, J. H., Gatley, I., Merrill, K. M., & Weintraub, D. 1994, ApJ, 421, 600
Lame, N. J., & Pogge, R. W. 1994, AJ, 108, 1860
Liu, X.-W., & Barlow, M. J. 1996, MNRAS, 279, 511
Liu, Y., Liu, X.-W., Luo, S.-G., & Barlow, M. J. 2004, MNRAS, 353, 1231
Malkov, Yu. F., Golovatyj, V. V., & Rokach, O. V. 1995, Ap&SS, 232, 99
Masson, C. R. 1990, ApJ, 348, 580
McCandliss, S. R., France, K., Lupu, R. E., Burgh, E. B., Sembach, K., Kruk, J., Andersson, B-G, & Feldman, P. D. 2007, ApJ, 659, 1291
Meaburn, J., Boumis, P., López, J. A., Harman, D. J., Bryce, M., Redman, M. P., & Mavromatakis, F. 2005, MNRAS, 360, 963
Meaburn, J., López, J. A., Gutiérrez, L., Quiróz, F., Murillo, J. M., Valdéz, J., & Pedrayez, M. 2003, Rev. Mex. AA, 39, 185
Meixner, M., McCullough, P. R., Haartman, J., Son, M., & Speck, A. K. 2005, AJ, 130, 1784
Mitchell, D. L., Pollacco, D., O'Brien, T. J., Bryce, M., López, J. A., & Meaburn, J. 2006, in IAU Symp. 234, Planetary Nebulae in Our Galaxy and Beyond, ed. M. J. Barlow & R. H. Mendez (Cambridge: Cambridge Univ. Press), 139
Napiwotzki, R. 1999, A&A, 350, 101
Napiwotzki, R., & Schönberner, D. 1995, A&A, 301, 545
O'Dell, C. R. 1998, AJ, 116, 1346
———. 2005, Rev. Mex. AA Ser. Conf., 23, 5
O'Dell, C. R., Balick, B., Hajian, A. R., & Henney, W. J. 2002, AJ, 123, 3329
O'Dell, C. R., & Burkert, A. 1997, in IAU Symp. 180, Planetary Nebulae, ed. H. Habing & H. J. G., L. M. Lamers (Dordrecht: Reidel), 332
O'Dell, C. R., & Doi, T. 1999, PASP, 111, 1316
O'Dell, C. R., Henney, W. J., & Ferland, G. J. 2007, AJ, 133, 2343
O'Dell, C. R., McCullough, P. R., & Meixner, M. 2004, AJ, 128, 2339
O'Dell, C. R., Weiner, L. D., & Chu, Y.-H. 1990, ApJ, 362, 226
Osterbrock, D. E. 1989, Astrophysics of Gaseous Nebulae and Active Galactic Nuclei (Mill Valley: University Science Books)
Pauldrach, A. W. A., Hoffmann, T. L., & Mendez, R. H. 2004, A&A, 419, 1111
Perinotto, M., Schönberner, D., Steffen, M., & Calonaci, C. 2004, A&A, 414, 993
Phillips, J. P. 2003, MNRAS, 344, 501
Pottasch, S. R. 1984, Planetary Nebulae: A Study of Late Stages of Stellar Evolution (Dordrecht: Kluwer)
Pottasch, S. R., & Preite-Martinez, A. 1983, A&A, 126, 31
Ragazzoni, R., Cappellaro, E., Benetti, S., Turatto, M., & Sabbadin, F. 2001, A&A, 369, 1088
Sabbadin, F., Benetti, S., Cappellaro, E., Ragazzoni, R., & Turatto, M. 2005, A&A, 436, 549
Sabbadin, F., Bianchini, A., Ortolani, S., & Strafella, F. 1985, MNRAS, 217, 539
Sabbadin, F., Cappellaro, E., & Turatto, M. 1987, A&A, 182, 305
Sabbadin, F., Turatto, M., Cappellaro, E., Benetti, S., & Ragazzoni, R. 2004, A&A, 416, 955
Sabbadin, F., Turatto, M., Ragazzoni, R., Cappellaro, E., & Benetti, S. 2006, A&A, 451, 937
Schönberner, D. 1983, ApJ, 272, 708
Speck, A. K., Meixner, M., Fong, D., McCullough, P. R., Moser, D. E., & Ueta, T. 2002, AJ, 123, 346
Speck, A. K., Meixner, M., Jacoby, G. H., & Knezek, P. M. 2003, PASP, 115, 170
Spitzer, L., Jr. 1978, Physical Processes in the Interstellar Medium (New York: Wiley)
Stanghellini, L., Villaver, E., Manchado, A., & Guerrero, M. A. 2002, ApJ, 576, 285
Steffen, W., & López, J. A. 2004, ApJ, 612, 319
———. 2006, Rev. Mex. AA, 42, 99
Turatto, M., Cappellaro, E., Ragazzoni, R., Benetti, S., & Sabbadin, F. 2002, A&A, 384, 1062
Tylenda, R., Acker, A., Stenholm, B., Gleizes, F., & Raytchev, B. 1991, A&AS, 89, 77
Tylenda, R., Stasińska, G., Acker, A., & Stenholm, B. 1994, A&AS, 106, 559
Vassiliadis, E., & Wood, P. R. 1993, ApJ, 413, 641
Vishniac, E. T. 1994, ApJ, 428, 186
Wang, W., Liu, X.-W., Zhang, Y., & Barlow, M. J. 2004, A&A, 427, 873
Williams, R. J. R. 1999, MNRAS, 310, 789
Wilson, O. C. 1950, ApJ, 111, 279